Nanoscale

PAPER

View Article Online
View Journal | View Issue

Cite this: *Nanoscale*, 2026, **18**, 384

Enhancing thermal conductivity and flame resistance of carbon fiber composites using CNT-infused multiphase graphene resins

Yogin Patel,*[a] Pei Huan Sun,[b] Bryan Llumiquinga,[a] Nandi Bao,[a] Jonathan Shi,[a] Adrien Duran,[a] Charm O. Nicholas,[a] Rituparna Mohanty,[b] Nare Cho,[a] Iris You,[b] Stephen D. Tse [a] and Jonathan P. Singer *[a,b]

Carbon fiber composites (CFC) are distinguished by their remarkable strength-to-weight ratio, rendering them exceptionally suitable for various applications. This study explores replacing the conventional polymer epoxy matrix in CFCs with macropore-infused graphene nanocomposite emulsion thermosets (MINETs) based on easily sourced materials. The explored MINETs are formed from epoxy resin, graphene particles, and different oils as working fluids. This approach allows CFCs to exhibit multifunctional properties, including enhanced thermal conductivity and flame resistance, making them ideal for fire-proof drone enclosures, electronic casings, and thermal-energy-storage equipment applications. The thermal conductivity was further increased by adding carbon nanotubes (CNT) to the MINET matrix. The rheological properties of MINET allowed for CNT loading concurrently alongside graphene, without preventing processing. Rheological evaluations and Vickers hardness assessments were conducted to optimize the maximum CNT loading for efficient molding and robust mechanical properties. Thermal conductivity analysis demonstrated that CNT-reinforced MINET composites have a higher thermal conductivity when compared to standard graphene-MINET formulations. Infrared thermal imaging confirmed that CFC MINET composites have better dynamic heat transfer properties than CFC epoxy samples. Flammability tests indicated an improved flame resistance, particularly for silicone oil CFC MINET CNT formulations. The results indicate that CNT-infused CFC MINET exhibits exceptional thermal management and enhanced fire resistance co-optimized with mechanical properties, thus rendering it ideal for high heat dissipation, thermal stability, and flame retardancy.

Received 29th August 2025,
Accepted 10th November 2025

DOI: 10.1039/d5nr03659c

rsc.li/nanoscale

1. Introduction

Carbon fiber (CF) is employed in composite fabrication, applied in automotive, defense, and aeronautics industries due to its superior strength-to-weight ratio, stiffness, and corrosion resistance. Its extensive usage is attributed to its ability to withstand significant mechanical loads while reducing structural weight.[1–3] Polymers are integral as binders and protective agents, ensure uniform load distribution, and safeguard fibers from environmental factors.[3] Carbon fiber exhibits a tensile strength of 3–7 GPa and a density of 1.6–2.2 g cm^{-3},[4,5] rendering it significantly lighter than steel or aluminum. These epoxy-reinforced composites enhance durability against fatigue cracks and oxidation, and their malleability allows for precise structural design.[6,7] However, limitations exist, notably the poor out-of-plane thermal conductivity and high flammability of epoxy resins used in composites, which are more prone to ignition at elevated temperatures, as evidenced by their high heat release rates (HRR).[8–10] In contrast, non-composited metals such as aluminum and titanium do not facilitate fire spread and do not emit toxic fumes, which is advantageous for environmental safety. Furthermore, traditional materials exposed to high temperatures can form a protective char layer that mitigates oxygen diffusion and heat penetration, a quality not shared by CF-based polymer composites, which tend to decompose rapidly and release flammable gases during combustion.[8]

These concerns can be mitigated to some extent through the addition of flame retardants or by increasing the thermal conductivity of the matrix by distributing the incident heat sources. However, the current state of flame-resistant additives faces several concerns. There is a push to replace traditional

[a]*Department of Mechanical and Aerospace Engineering, Rutgers University, Piscataway, NJ 08854, USA. E-mail: ykp11@rutgers.edu, jonathan.singer@rutgers.edu*
[b]*Department of Materials Science and Engineering, Rutgers University, Piscataway, NJ 08854, USA*

halogen-based retardants, which are highly effective but detrimental to the environment.[11] Phosphorous-based retardants, which are more environmentally friendly and exhibit good flame retardancy characteristics, face several processing issues.[12] Inorganic phosphates such as ammonium polyphosphate, melamine phosphate, and melamine pyrophosphate tend to have poor compatibility with epoxy resins and will settle after mixing, affecting the flammability of the materials.[13] More promising flame retardants such as the derivatives of 9,10-dihydro-9-oxa-10-phosphaphenanthrene-10-oxide (DOPO) have exhibited reduced mechanical properties due to migration and leaching.[12] Zhang *et al.* was able to incorporate DOPO into the epoxy resin backbone, however this impeded complete cross-linking of the polymer.[14,15] Current research into DOPO is focused on incorporating DOPO with various other flame retardant materials.[16]

Past research studies have indicated that incorporating graphene and carbon nanotubes (CNTs) into multiphase polymer matrices can effectively mitigate these concerns due to their superior thermal stability and reinforcement properties.[17,18] Graphene-coated fabrics can achieve thermal conductivities as high as 9.5 W (m K)$^{-1}$ when applied to substrates, demonstrating substantial improvements in heat dissipation capabilities.[19] Graphene facilitates the formation of an organized carbonaceous layer on the composite surface, serving as a barrier to heat and oxygen diffusion, thereby lowering the HRR below 500 °C, indicative of significant flame retardancy.[20] Graphene has also been combined with flame retardant additives such as melamine phosphate or DOPO to improve thermal, mechanical, and flammability properties.[21] CNTs exhibit remarkable mechanical, electrical, and thermal characteristics, rendering them effective for reinforcement. They establish a protective network that decelerates flame propagation and enhances the mechanical integrity of the polymer matrix while augmenting flame resistance.[22] CNTs modified with melamine polyphosphate can double the thermal conductivity of composites from 0.21 to 0.42 W (m K)$^{-1}$ while simultaneously improving flame retardancy.[23] CNT performance is typically limited by the dispersion of the particles within the polymer matrix, but Chen *et al.* were able to modify CNTs into a well-dispersed matrix with a reactive hyperbranched polyphosphoramide.[24] A study examined the synergistic effect of CNTs and graphene on flame-retardant properties within a polypropylene matrix, achieving a 31% oxygen index and an 83% reduction in HRR, with an ignition delay of 40 seconds relative to pure polypropylene.[18] Thus, it is evident that building 3D thermally conductive nanofiller networks in polymer composites is an effective way to enhance their thermal conductivity. The method of adding complex chemicals continues with CFCs, incorporating reactive fire retardants such as DOPO or branched polyethyleneimine and ammonium polyphosphate within the polymer matrix while mechanically supported by the carbon fibers.[16,25] Although effective, these methods focus on chemically intensive methods with highly specialized ingredients, and conventional fabrication techniques, such as chemical vapor deposition,[26] freeze-drying,[27] and self-assembly,[28] are hampered by complex processes and the need for sophisticated equipment. These factors reduce the likelihood of integration into high output industrial processes for the current state of the art in CFC flame retardant research.

Here, we explore macropore-infused nanocomposite emulsion thermosets (MINETs) as a CFC polymer matrix co-optimized for thermal and mechanical properties.[29] MINETs are formed when two immiscible liquids, a surfactant, and particles are mixed at high shear to create a bi-continuous structure of the fluids. Here, epoxy and working fluid (oil) are used as the two immiscible liquids, and a suitable surfactant is identified. Fig. 1 provides a schematic illustration of the preparation and structure in which the surfactant plays a role in stabilizing the emulsion along with enhancing the nanoparticle dispersion, thereby ensuring a well-structured composite. With the addition of microparticles and mixing at high shear, the viscosity of the emulsion is increased, and macrophase separation is prevented during curing, maintaining structural integrity without significant shrinkage.[29]

MINET structure has (1) an epoxy phase that provides the required mechanical strength and structural integrity, (2) an oil phase that acts as a porogen, which introduces tunable porosity, and (3) a particle phase that reinforces the material and improves the functional properties.[29] This engineered porosity results in a lighter, more heat-resistant, and mechanically tunable material, distinguishing it from conventional dense polymer matrices. Here, higher particle loadings are balanced by the working fluid to achieve desirable viscosity, allowing a thermally conductive particle phase with a higher flame-retardant oil phase. For thermal MINETs, graphene and CNT are among the best particle options, which will be tested further with canola oil and silicone oil to check their fire resistance behavior. Combining these materials with CFCs will allow the selection of the desired multifunctionality. This study aims to identify the properties of MINET-based CFCs compared with conventional CFCs while enhancing heat dissipation, flame retardancy, and multifunctionality, thereby addressing deficiencies in thermal management, thermal shock resistance, and material adaptability.

2. Experiment section

2.1 Materials

All materials were used as received. Graphene platelet (6–8 nm thickness and <2 μm long particles) powder was procured from Skyspring Nanomaterials. A scanning electron microscopy (SEM) image of the associated graphene particles is shown in Fig. S1. 105 Epoxy Resin (major component propane, 2,2-bis[*p*-phenyl]-, polymers) and 206 Slow Hardener (polyoxypropylenediamine mostly) were procured from West System. The mix ratio is five parts of the resin to one part of the hardener by weight. Arkema Chemical and Plasthall provided epoxidized soybean oil (Vikoflex 7170). Canola oil and silicone oil were procured from Sigma–Aldrich. The silicone oil surfactant, dimethylsiloxane block copolymer (DBP-732), was obtained from

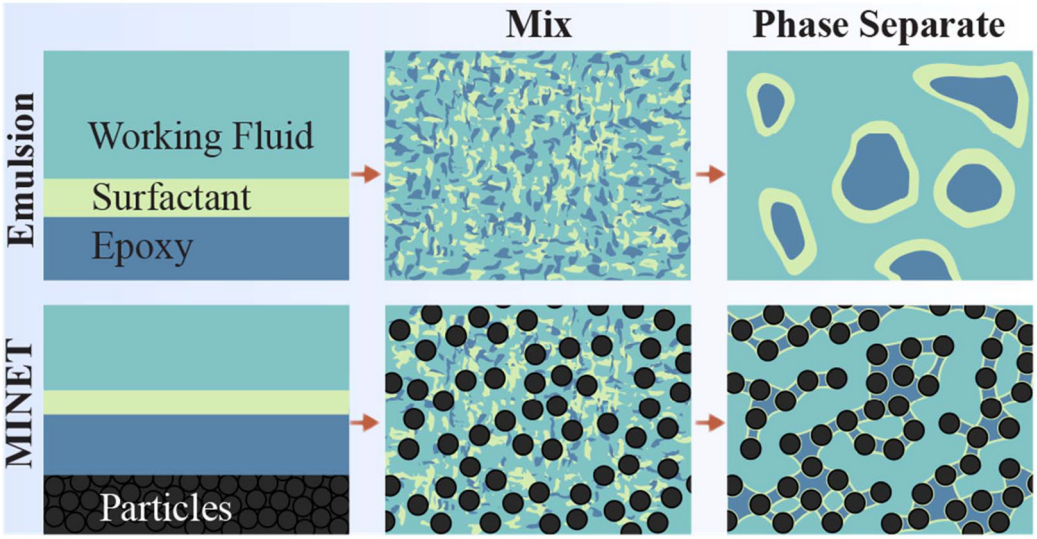

Fig. 1 Schematic of MINET preparation and concept. A non-MINET ternary liquid system (epoxy-surfactant-working fluid) forms an emulsion after mixing due to phase separation (top). By contrast, in MINET, the ternary system becomes a bicontinuous gel where the morphology is arrested by nanoparticle jamming but can still be processed. Schematic is modified with permission from Wiley.[29]

Gelest. Carbon fiber fabrics (3 K, plain weave pattern, 0.012-inch thick carbon fibers) were procured from Fibre Glast. CNTs were acquired from Huntsman (Miralon powder).

2.2 MINET fabrication

The MINET fabrication process involved mixing 105 epoxy resin, 206 cross-linker (hardener), ESO, canola oil, and particles for vegetable oil-based MINETs. Similarly, silicone oil-based MINETs were prepared using 105 epoxy resin, 206 hardener, DBP-732 surfactant, silicone oil, and particles. The final epoxy composite mixture was homogenized using a speed-mixer (FlackTek DAC150.1 FVZ-K) at 3500 rpm for 2 min. Depending on the compositions, the MINETs were cured at ambient conditions for 16–24 hours. For porosity analysis, the canola and silicone oil were removed by solvent hexane immersion for >12 hours, followed by ambient drying for >24 hours. This resulted in an interconnected porous network throughout the epoxy-nanocomposite matrix. MINET was considered optimal when the entire oil phase was removed without removing other components (as determined by mass loss). In idealized MINET, as shown in Fig. S2, a favorable solvent amount removes the continuous oil phase generated by macrophase separation.

2.3 MINET structure fabrication

Two types of templates were used for molding the different MINET structures: (1) 3D printed PLA templates for the rectangular samples (20 mm (L) × 6.75 mm (W) × 6.75 mm (H)) and (2) silicone rubber cylindrical shaped templates (31.75 mm diameter × 10 mm) for measurement of thermal properties. The uncured MINET or epoxy composite lump was placed on a concave impression-shaped template. The template (with MINET on top) was placed between two parallel plates and further placed within the platens of the vice. Embossing pressure drove the soft MINET to flow and fill the template cavities. The MINET template assembly was kept at room temperature for 16–20 hours (depending on composition) to complete MINET curing. The rectangular mold samples were cured (20 hours) uniformly in a vise press to measure mass loss and porosimetry and perform flammability testing.

2.4 Sample characterization

To characterize the porosity, SEM (Zeiss Sigma FESEM with Oxford EDS), mercury intrusion porosimeter (Micrometrics 9610), and micro-CT (Bruker SkyScan 1272 CT) were used. The same SEM was also used to characterize the silica phase after burning *via* electron dispersive spectroscopy (EDS). A rheometer (Malvern Kinexus Ultra+) was used to measure the rheological properties of MINET. The samples were loaded quickly after shear mixing (typically <10 min). The high-resolution micro-CT was performed with a spatial resolution of 0.7 μm and an image size of 4904 × 3290 using a 5kX camera. Vickers hardness value is calculated by measuring the indentation on the cylindrical composite samples using a Leica optical microscope.

2.5 Sample preparation for thermal conductivity measurement

For all epoxy composites, based on the viscosity, the uncured material was poured into two flat-bottomed cylindrical silicone molds and cured at room temperature for 20 hours. The cured samples were further removed by detaching the silicone templates. Thermal conductivity measurements were taken using a Hot Disk TPS 500 Thermal Constants Analyser at room temperature (25 °C) under controlled environmental conditions to

minimize the external influence on the results. During the measurement, the Hot Disk sensor is sandwiched between one sample and one sample holder, ensuring optimal thermal contact and reliable data collection. This measurement is used to determine the thermal conductivity through an automated curve fitting analysis. This fitting uses specific heat as a parameter, though not as robustly as the thermal conductivity, and a physical range of heats (0.5–2 MJ m^{-2} K) was ensured.

2.6 CFC MINET sample fabrication

Uniform MINET samples were prepared using a speed-mixer to fabricate the CFC MINET samples. The resulting MINET was incorporated homogeneously as a matrix material with a single carbon fabric ply. This single sheet of carbon fiber fabric was folded again in half to create two layers. MINET material was also applied again, and this double-layered fabric was folded in half again, resulting in a four-layer carbon fabric composite structure (2 × 2 inch size). The resultant CFC MINET composites were mounted between flattened plates of vice. CFC samples were cured further for 24 hours at ambient conditions under the assumption that the samples were molded homogeneously without any entrapped air bubbles. This methodology ensures that the MINET mixture is evenly distributed between each layer, creating continuous intricate networks throughout the composite. The CFC MINET sample was used to measure the thermal conductivity using the same procedure mentioned previously for the MINET sample.

2.7 CFC composite sample for temperature measurement using a thermal camera

The thermal behavior of the composite samples was characterized using a Seek Shot Pro thermal camera, which provides real-time temperature measurements and thermal imaging capabilities. The experimental setup consisted of a hot plate as the heat source, maintained at precise temperatures to ensure consistent and controlled heating conditions. Each composite sample was placed directly on a hot plate surface. The temperature measurements were recorded spontaneously through the reference point on the sample surface and hot plate(5 inches from the sample surface and camera front) at 5 minute intervals and for 37 minutes. Square glass (1 × 1 cm and 0.1 mm thickness size, placed on the sample surface) was used for its near-zero thermal expansion coefficient and dimensional stability at high temperatures. It ensures consistent temperature readings across samples of varying thicknesses by creating a uniform contact surface for measurement and uniform measurement emissivity. All measurements were performed under ambient room air conditions (~25 °C).

2.8 Flammability test on epoxy and CFC composites

The flame test was performed on the epoxy and CFC composites using a modified ASTM D635 test, which quantifies a rate at which a sample burns when exposed to a flame in a controlled environment. All sample tests were conducted in a fume hood (controlled laboratory environment) to ensure proper ventilation and safety protocols. CFC samples were cut precisely into rectangular shapes (1.5 × 0.5 inches) and mounted horizontally on a sturdy metal clamp in a vertical orientation. A calibrated burner (Bernzomatic) was ignited to generate a steady blue flame (~430 °C) for sample burning. The burner was then positioned at a 45-degree angle to the sample's surface, with the flame tip touching the lower left corner of the sample. The flame was exposed to the sample surface for 30 seconds after ignition, and the flame spread rate was observed. The flame was removed after 30 seconds, and the time and extent of burning were recorded. The samples were naturally cooled, and visual inspection was performed to evaluate burning damage. The flame spread rate and extent of damage were observed to evaluate the performance differences between the various composite formulations.

2.9 Statistical analysis

The results in Fig. 3b, 4b and c are based on the mean and standard deviation of $n = 5$ samples. Other results were from individual samples, where data trends were identified by testing multiple experimental conditions. The results in Fig. 3c and 4a were normalized to the total component mass.

3. Results and discussion

3.1 Processability, hardness, and porosity of graphene MINET and MINET CNT samples

The MINET formulation procedure was initially conducted using silica and super-activated carbon particles. It was observed that the characteristic size of the pores is directly correlated with the dimensions of the particles employed.[29] Similar trends are anticipated in other particles should be well dispersed; however, the implications of incorporating anisotropic flakes, such as graphene, remain unclear.[30] The MINET samples were further prepared with graphene particles (measuring 6–8 nm thickness), epoxy, and working fluid (canola and silicone oil) with surfactant. The right amount of surfactant was selected by examining the phase properties of the final composite through mass loss and porosimetry analysis (Fig. S2).

After mixing all the components with a high shear, this MINET matrix exhibits putty-like rheological behavior and can flow into narrow shapes (as illustrated in Fig. 2a) when extruded through a needle. Additionally, it is amenable to molding from larger macro shapes to centimeter-scale dimensions (Fig. 2b). By leveraging this conventional resin-like viscosity, it can be easily molded in conjunction with a CF structure (Fig. 3a). For the local pore structure evaluation, computed tomography (CT) scan images were acquired from the cross-sectional area of the CFC epoxy control sample and CFC MINET structure, as depicted in Fig. 2d and e, respectively. The objective is to uncover the differences in pore size and structure resulting from forcing the MINET material into the inter-fiber spacing. The preservation of the continuous pore networks is further corroborated by the SEM image in Fig. 2f. Mercury porosimetry will be employed for global assessment,

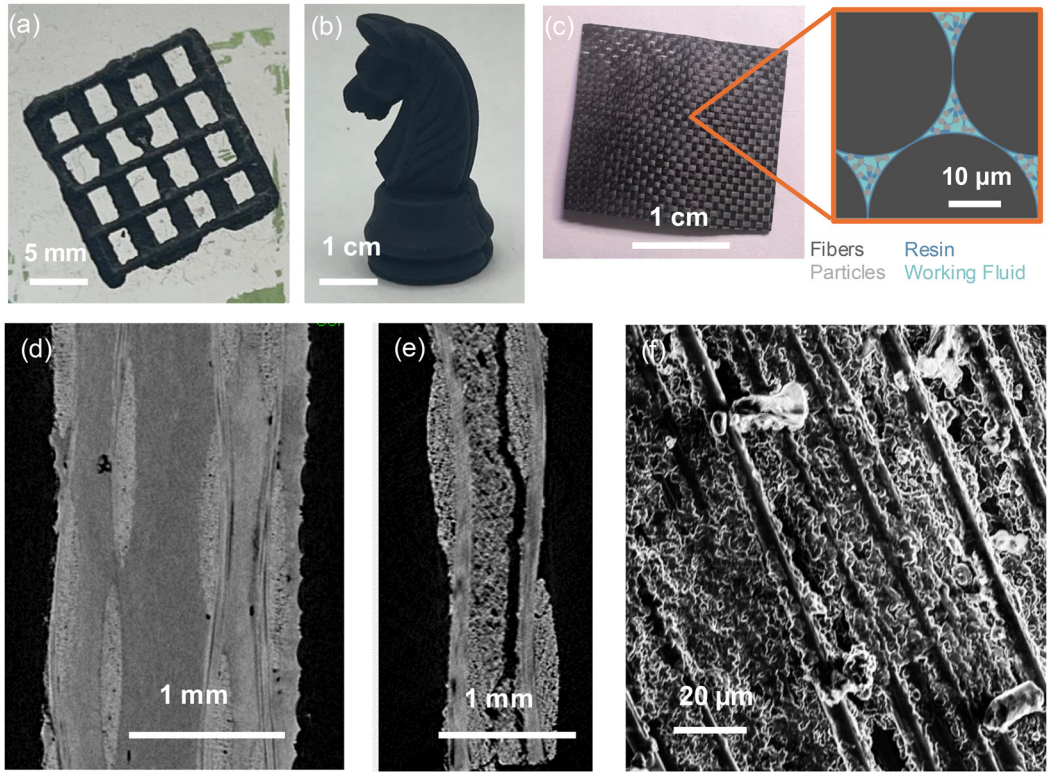

Fig. 2 (a) Photograph of graphene MINET print through needle extrusion. (b) Photograph of the molded graphene MINET structure. (c) A photograph of molded MINET-CF composite and a schematic inset of the presumed structure is drawn roughly to scale. CF (dark grey) was molded with MINET resin from graphene nanoparticles (light grey), surfactant, epoxy, particles, and working fluid. Comparison of CT images of (d) conventional CFC control and (e) CFC MINET sample (without oil phase), and (f) SEM image of CFC graphene MINET (without oil phase).

which will elucidate how the pore size distribution diverges from that of the bulk MINET.

Graphene is an attractive particle for MINET formulation due to its efficient heat transfer through phonon-driven lattice vibrations.[31,32] However, excessive graphene content increases viscosity, affecting the rheological properties and structural uniformity due to agglomeration, high surface area, and strong van der Waals forces. High viscosity hinders processability, affects porous structures, and reduces compatibility with carbon fabrics during molding. These results agree with previous studies that reported viscosity challenges in particle-based composites at high optimal loadings.[29]

One solution to this processability problem involves combining CNTs with graphene to create hybrid structures that leverage the properties of both materials. Incorporating CNTs into MINET samples enhances their thermal conductivity and electrical properties.[33] Compared to graphene particles, CNTs have a lower density, which allows improvement in material properties upon small mass addition.[34] This is particularly helpful when used to mitigate viscosity problems at high graphene particle concentrations. Therefore, minimal CNT loadings are necessary to optimize processing and subsequent compatibility with CFC.[35]

A relatively small amount of CNT (~2 wt%) was used to formulate MINET samples. Further, this addition of CNTs did not affect the viscosity of the MINETs to a degree that changed the molding properties. By contrast, it was impossible to make controls with the same loading of graphene and CNT without forming a MINET (*i.e.*, adding oil and surfactant). To quantify this, rheological analyses were performed on the epoxy composites (Fig. 3a). The compositions of the different epoxy composites are listed in the SI (Table S1). MINET compositions were selected based on preliminary electrical conductivity studies as providing co-optimized conductivity and processability (Fig. S3). All samples exhibited a higher shear viscosity than the pure epoxy control sample at shear rates ranging from 0.1 to 100 s^{-1}. Additionally, at high shear approaching 100 s^{-1}, MINET composites had lower shear viscosity than the Epoxy Graphene sample, which contained epoxy and graphene particles only. This is despite the fact that the control had less graphene than the MINETs (13% *vs.* 21%), with higher control loadings proving too viscous to be processed. In all other composites, the viscosity reduced with increased shear rates (0.1 to 10 s^{-1}), and the viscosity curve decreased further (at a shear rate beyond 50 s^{-1}), which displayed a shear-thinning phenomenon. Similar composite systems exhibit this behavior primarily because of the increased interparticle bonding at higher particle concentrations.[30] Notably, the addition of CNT does not affect shear thinning, which allows for facile MINET processing compared to other composites with higher CNT or

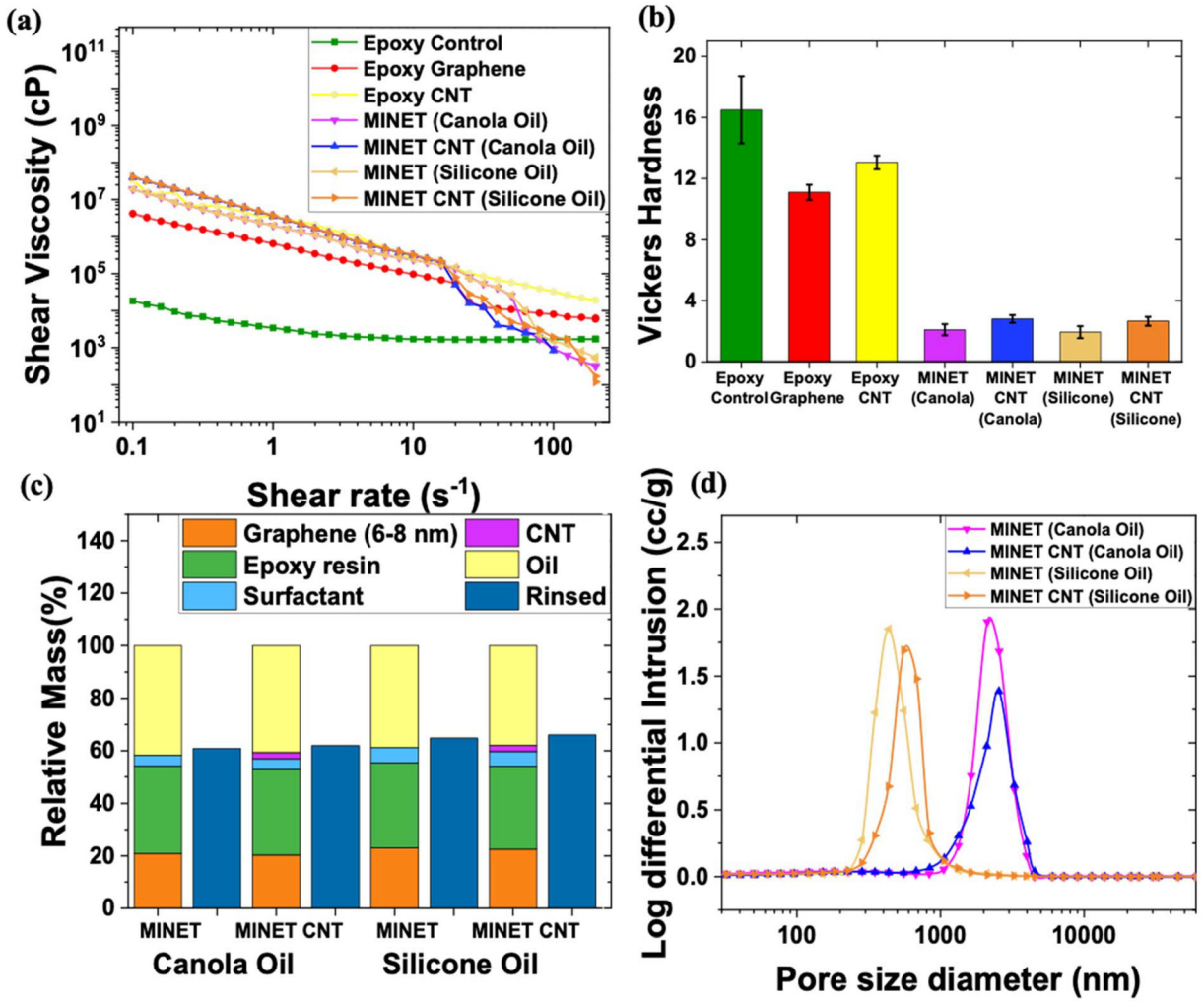

Fig. 3 (a) Rheology and (b) Vickers hardness test results for different epoxy and Graphene MINET and Graphene MINET CNT composites. (c) Mass loss for individual epoxy composite samples with canola and silicone oil as working fluids, as shown by component masses (left bar) and mass of final composite after hexane rinsing (right bar). Both are normalized to the total component mass. (d) Mercury porosimetry results for the samples are shown in (a). The curves represent the change in intruded pore volume, $dv/d\log(d)$, as a function of pore diameter, d.

graphene concentrations. Further, we were unable to identify CNT bundles or agglomerates in electron micrographs of polished cross-sections of the MINET CFCs, suggesting that they were well-distributed in the matrix (Fig. S4).

As shown in the Vickers hardness test (Fig. 3b), MINET samples are much softer than the other epoxy (control) and epoxy particle samples due to the oil content in the MINET. A similar trend (Table S2) was observed with the CFC-MINET sample, which exhibited a lower tensile modulus compared to the standard CFC control. However, a smaller addition of CNT increased the hardness of the samples compared to those without CNT, indicating that CNTs strengthen the matrix without diminishing its processing properties. Further, these new materials can be integrated with conventional CFCs as top layers (as shown in Fig. S5), allowing for a thermally conductive (and thereby protective) skin. After removing the oil content, the mass loss of the samples was further analyzed (Fig. 3c). The mass loss of the canola oil MINET sample (42% oil content) was approximately 39%, and for the silicone oil MINET (39% oil content) was about 35%. However, a lower mass loss was observed for the MINET CNT samples after oil removal process. Rinsed canola oil MINET CNT samples had 38%, and silicone MINET CNT samples had 34% mass loss compared to their initial oil contents (around 41% and 38%, respectively). These results suggest a stronger bonding interaction between the CNTs and adjacent particles to prevent the removal of oil particles during the oil extraction process.[36]

To validate the existing microporous network structure of graphene MINET and MINET CNT, mercury porosimetry was performed afterward on the same rinsed and porous samples generated by the mass loss procedure (Fig. 3c). The results show that although the average pore sizes of the two composites were similar, the pore volume of the CNT-added sample decreased. The observed reduction in the alignment

probability reinforces the distribution of CNTs into the larger pores in the composite structure. This was further confirmed by the improved bonding characteristics of CNTs in the composite structure,[37] along with the retention of oil particles within the samples. Fig. 3d also indicates that silicone oil MINET samples have smaller pore sizes than canola oil MINET samples, which confirms improved small porous networks generated using silicone oil-based MINET procedure.

3.2 Thermal conductivity measurements for different epoxy composites

The thermal conductivity measurements demonstrate the significant enhancement achieved by incorporating graphene MINETs and CNTs into CFCs, as shown in Fig. 4a and b. The Epoxy CNT sample had twice the thermal conductivity value compared to the Epoxy control sample and 60% lower than the Epoxy Graphene (13 wt% graphene) sample due to higher graphene particle loading. Graphene MINET displays ~10% greater thermal conductivity than the Epoxy Graphene control due to its higher graphene content. The thermal conductivity exhibited by the MINET CNT variant shows an increase of ~40% when contrasted with the conventional MINET sample without CNT inclusion. This favorable enhancement of the thermal management properties of the composite suggests the considerable effectiveness of CNTs in improving the heat transfer power of the composite. As in the case of the inclusion of CNT in polymer matrices, similar enhancements in thermal conductivity due to CNT inclusion have been reported in previous studies.[38] Among the MINET CNT samples, silicone oil-based samples had ~5% lower in-plane thermal conductivity than canola oil samples.

Nevertheless, both samples showed thermal conductivity values independent of the working fluid when rinsed, indicating that the oil phase is crucial in contributing to the thermal properties. The thermal conductivity of rinsed samples was also lower (~1.5 *vs.* ~1.7), resembling the properties of the Epoxy Graphene sample, due to the reduced thermal conductivity of air-filled pores as opposed to oil-filled pores. The reduction in thermal conductivity is slightly greater than what might be expected from removal of approximately 40% of 0.2 Wm^{-1} k^{-1} volume from the parallel model for continuous composites (which would predict a reduction of 0.08 Wm^{-1} k^{-1}), but this is consistent with other porous materials due to the effects of tortuosity and increased impedance of the drained pores.[39]

The samples were processed with CFC, further contributing to heat transfer through their inherent conductive properties. The thermal conductivities of the CFC samples (Fig. 4c) were greater than those of the epoxy composites alone. Among all the samples, the CFC MINET CNT samples have the highest thermal conductivity. This outcome highlights the synergistic effect of all components, where CNTs and graphene particles aid in electron conduction, and carbon fibers enhance heat propagation in the composite. Similarly, the thermal properties of hybrid composites with highly conductive fillers (CNTs and graphene) have exhibited similar trends.[35,40] One notable aspect to consider is that the thermal measurement approach used here (Hot Disk TPS) measures effects arising from both in-plane and out-of-plane thermal conductivity. Since the in-plane thermal conductivity of CFCs is much higher due to conduction along the fiber,[41] it is anticipated that the enhancement is primarily coming from out-of-plane/fiber-to-fiber conductivity.

3.3 Out-of-plane thermal performance of CFC samples

Thermal conductivity measurements provide valuable insight into composite static heat transfer capabilities; however, thermal camera measurements provide a dynamic, real-time view of the heat distribution and temperature evolution across the samples and, in this particular case, the out-of-plane response. Fig. 5a illustrates the thermal camera analysis that completes the static data of the thermal conductivity by showing how fast and evenly heat distribution can extend in the material.

Infrared imaging was used to characterize the steady-state thermal conductivity and transient thermal response of the

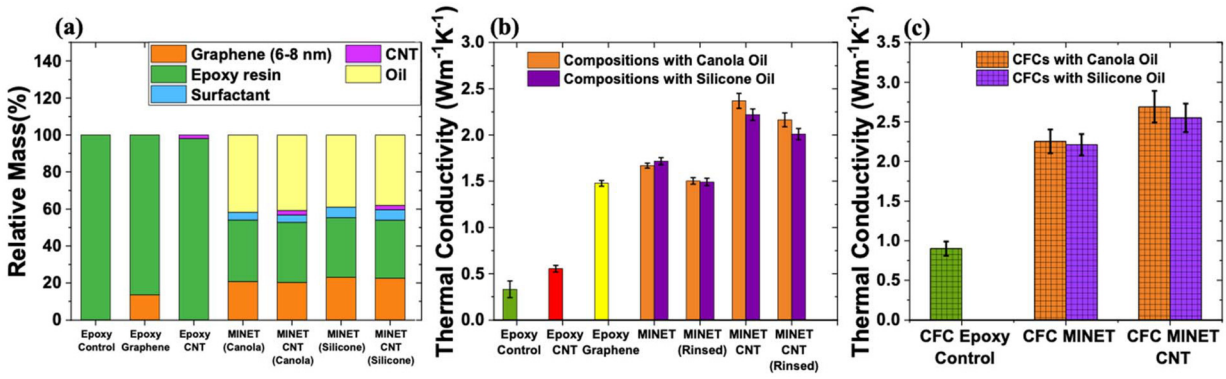

Fig. 4 (a) Different epoxy composites and their relative mass comparison. Hot disk TPS 500 thermal constants analyzer measured thermal properties of (b) different epoxy, graphene MINET, and MINET CNT and their rinsed samples (c) and CFC MINET samples for canola and silicone oil as working fluids.

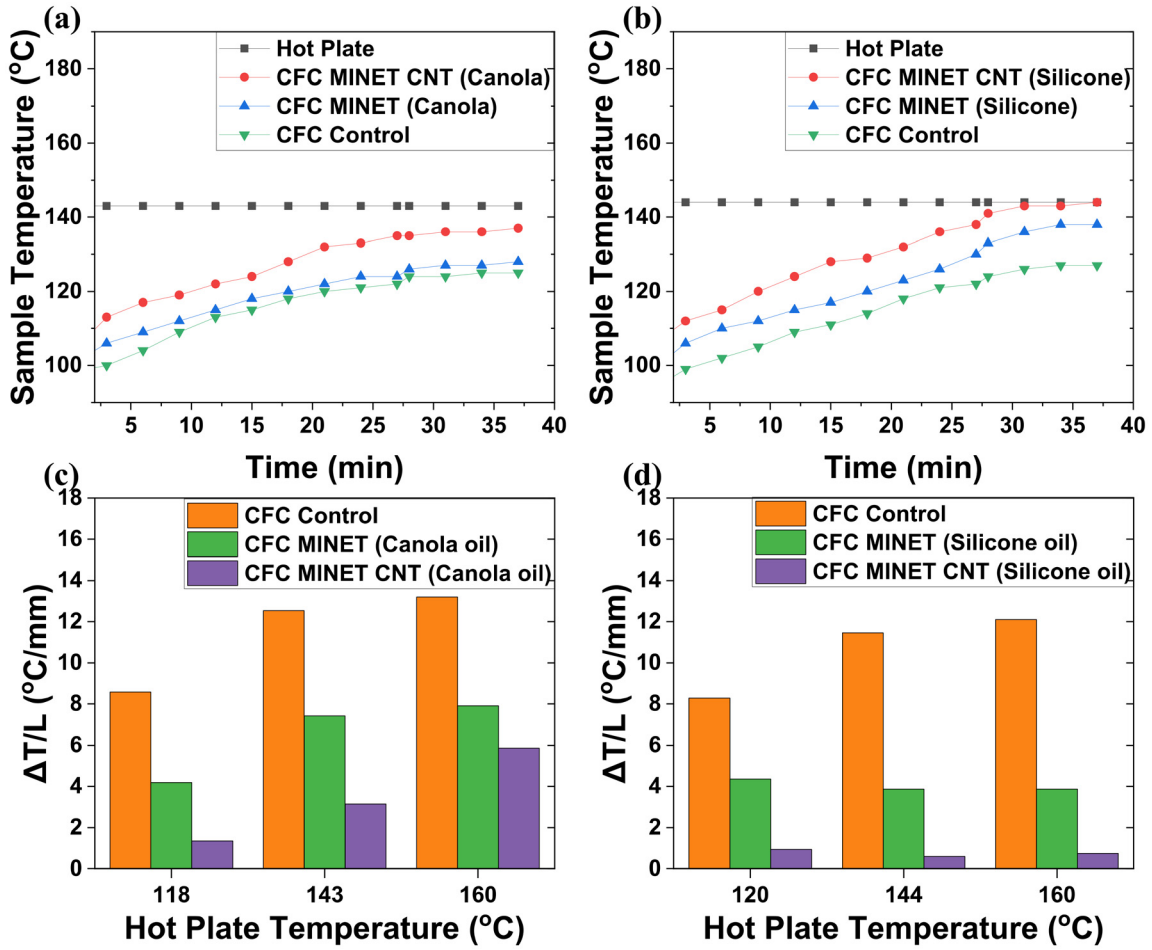

Fig. 5 Infrared Thermal camera setup measures the transient out-of-plane thermal response of three different CFC samples and hot plate. Comparison of temperature plots (at hot plate temperature 143 °C) generated using an infrared thermal camera for CFC control, CFC MINET, and CFC MINET CNT samples with (a) canola oil and (b) silicone oil as working fluids. Temperature gradient over thickness ($\Delta T/L$) for different CFC composites at three different hot plate temperatures for (c) canola oil and (d) silicone oil-based CFC samples.

samples, allowing a more comprehensive exploration of their thermal behavior. Thermal camera measurements revealed significant differences in the heat transfer behavior among different CFC samples. In particular, the temperature profiles of CFC MINET and CFC MINET CNT are compared with CFC control samples under steady heat at a hot plate temperature of 143 °C. Fig. 5a and b display the thermal behavior of CFC samples with canola oil and silicone oil as working fluids, respectively.

The temperature profile illustrates that the CFC MINET CNT demonstrates superior thermal conductivity in comparison to CFC MINET, which, in turn, exhibits greater thermal conductivity than the CFC control sample. Among the oil-based groups, CFC MINET with silicone oil samples (Fig. 5b) consistently outperformed canola oil-based compositions (Fig. 5a). The temperature curves of the silicone oil samples are steeper and achieve higher final temperatures (indistinguishable from the hot plate). CNT combined with silicone oil showed additional improvement in thermal performance, which is even more impressive when considering the synergistic effect that emerged between the CNTs and silicone oil to enhance the heat management performance of the composite.

To further investigate the thermal characteristics of the CFC samples, they were subjected to three different elevated temperatures on a hot plate, and the results for the temperature characteristics are shown in Fig. 5c and d. To reduce the effects of sample thickness, the temperature difference was normalized by the thickness ($\Delta T/L$) after a 31 minute exposure to the heat source. It should be noted that the thermal profiles are not expected to be linear in a fixed-open thermal profile; however, this allows for comparison. Again, the best heat conduction was observed in the CFC MINET CNT. The CFC control sample exhibited higher temperature gradients, and its value increased with the hot-plate temperature (8 to 13 °C mm^{-1}). The thermal gradients for canola oil CFC MINET and CFC MINET CNT samples were lower (4–8 °C mm^{-1} and 1–5 °C mm^{-1}, respectively), implying better heat distribution but lower efficiency than the silicone oil-based composites. Rather than any effect of thermal conductivity, this demonstrates the higher boiling point of the silicone oil, with canola

samples observed to have "dried" surfaces after the prolonged exposure approaching the smoke point of the oil (~200 °C).

3.4 Flammability test of different Epoxy and CFC samples

Burning tests were employed to evaluate the response of MINET and MINET CFCs to extreme thermal spikes compared with conventional epoxy (control) samples. Epoxy has poor flame resistance, which makes conventional CFC samples easily damaged by thermal spikes. Fig. 6a (also Movie S1) shows that the epoxy control sample burns at a high rate and the flame spreads uniformly across the entire sample. A similar behavior was observed in the CFC control sample (Fig. 6f and Movie S6), where the epoxy matrix material provided flame pathways and the post-burned CFC structure was damaged and delaminated. However, the inclusion of carbon fibers plays a significant role in heat distribution and flame resistance.

In contrast, Fig. 6b and c (also, Movies S2 and S3) show the flammability tests on graphene MINET samples (with and without canola oil) at different time intervals. It can be observed that flame propagation is reduced in the MINET structure with oil. This suggests that vegetable oil functions to prevent oxygen infiltration and acts as a source of latent heat, impeding the advancement of flame propagation until the temperature reaches the ignition threshold of the oil.

Silicone oil has high boiling and burning points, primarily due to its strong Si–O bonds and the formation of protective layers during combustion. These properties make silicone oils ideal for applications that require high thermal stability and fire resistance.[42,43] When exposed to fire, silicone-based coat-

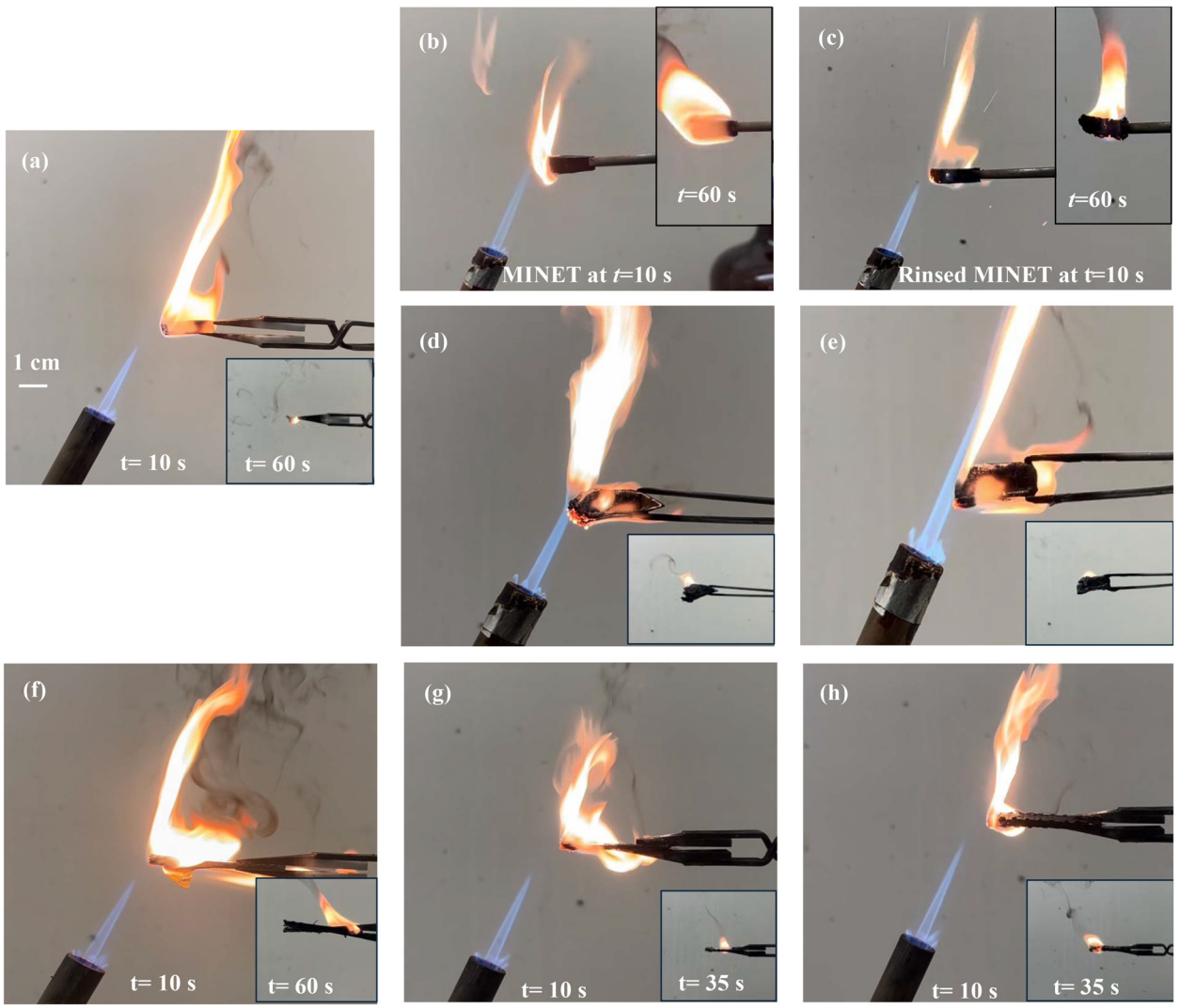

Fig. 6 Flammability test for (a) epoxy control (b) graphene MINET sample (with canola oil) and (c) graphene MINET sample (rinsed-without canola oil). Flammability test for (d) graphene MINET (silicone oil) sample without CNT, and (e) MINET CNT sample. The sample with CNT shows less radiation at the heated point. Flammability test for (f) CFC Epoxy control, (g) CFC MINET (silicone oil) sample without CNT, and (h) CFC MINET CNT sample. All burn test sample snapshots are shown at 10 s after heat source application, with the 60 s shown in the inset except in (g) and (h), where inset figures are at t = 35 s.

ings form a dense silica char layer that insulates the underlying material from heat and oxygen, thereby preventing further combustion.[44,45] This is apparent in the burning tests of MINET and MINET CFC shown in Fig. 6d and g (Also, Movies S4 and S7). The presence of silicone oil within the porous structure serves as a reservoir of latent heat, similar to canola oil, thereby impeding the progression of flame propagation until the temperature reaches the ignition threshold of the oil. The silicone oil underwent conversion into a white silica skin layer observable at the sample's forefront (Fig. 7a). While this layer is highly fragile, it could be observed in isolated fibers to not significantly change the fiber size and was confirmed to be silica through X-ray and infrared spectroscopy (Fig. 7b and Fig. S6). This further removes the fuel and ignition pathways for the propagating flame.[44,46] The transformation of the material leads to additional thermal resistance, which boosts its flame-retardant properties while preventing complete combustion. In both MINET and MINET CFC, the graphene particles also allowed heat transfer along the composite, suppressing ignition and burning compared with conventional epoxy (control) samples.

The thermal conductivity and heat distribution performance of the MINET composite material benefit significantly from the inclusion of CNTs. Fig. 6e and h (Movies S5 and S8) show that the CNT sample sustained better temperature spikes and visibly removed hotspots from the region under the direct flame. The distributed heat network formed by the CNTs regulated the thermal distribution while ensuring that the composites remained free from ignition.

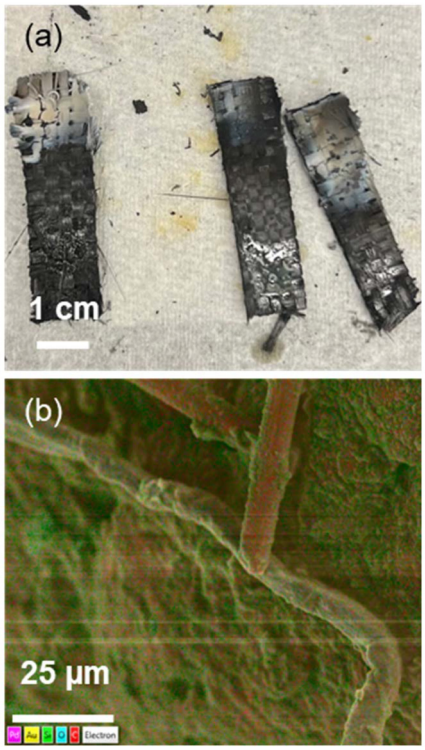

Fig. 7 (a) Silicone oil CFC MINET-CNT samples after burning experiments showing scattering silica skins at the top burnt surface. (b) SEM image with energy dispersive spectroscopy overlay of a fiber on the outer surface of a burnt CFC MINET-CNT. While the fiber appears uniform in the SEM scan, the portion closer to the top of the image shows predominantly carbon elemental signature, while the rest shows both silicon and oxygen. This is indicative of a region where the fragile silica layer was removed during the SEM sample preparation. Concurrently, the background composite uniformly shows silica from the char. It should be noted that this sample is coated in gold-palladium, leading to these residues in the spectra.

4. Conclusion

Combining graphene MINET with CNTs and silicone oil achieved the maximum performance in both the base epoxy resin and CFC. Silicone oil working fluid reduces combustibility through a silica conversion pathway, while the synergistic behavior of CNTs and graphene improves thermal redistribution. The modified composite materials exhibited exceptional fire resistance properties, making them promising candidates for high-performance applications requiring thermal stability with flame protection elements. While this comes at the cost of a reduction in stiffness, MINET CFCs can be integrated with conventional CFCs as a top protective layer with minimal additional processing steps or exotic additives. This makes MINET composites with CNTs and silicone oil promising candidates for large-scale use in electronics, aerospace, and other applications that require advanced thermal management systems with high thermal performance and flame retardancy. Future studies will evaluate the long-term durability of these combined MINET CFC-conventional CFC multilayers in application-relevant environments, as well as incorporate additional flame-retardant additives to the MINET system. Other applications may be possible by tuning the MINET system with different working fluids and particles to control various properties.

Conflicts of interest

J. P. S. is inventor on a patent application on MINET materials. The rest of the authors declare no conflict.

Data availability

The data supporting the conclusions of this study are included the article and the supplementary information (SI). Supplementary information: the compositions of the different epoxy composites and MINETs are listed in Table S1. An SEM image of the associated graphene particles is shown in Fig. S1. The mass loss and pore size distribution of MINET samples with different surfactant wt% are shown in Fig. S2. Mechanical properties of CFC composites are listed in Table S2. Fig. S3 shows electrical conductivity and shear plate measurements from a preliminary study of graphene-based MINETs. Fig. S4

shows SEM images of polished cross-sections of silicone oil CFC MINET-CNT. Fig. S5 shows a photograph of a CFC MINET sample molded with commercial prepreg fibers. Fig. S6 shows FTIR results for burned silicone oil MINET samples and silica nanoparticles. Movies S2 and S3 show the burn testing of MINET samples with and without canola oil, respectively. Movies S1, S4 and S5 present the burn testing of the epoxy control, MINET with silicone oil, and MINET-CNT with silicone oil, respectively. Movies S6, S7 and S8 display the burn testing of the CFC control, CFC MINET, and CFC MINET-CNT samples, all infused with silicone oil. See DOI: https://doi.org/10.1039/d5nr03659c.

Acknowledgements

This work was primarily supported by the Office of Naval Research through the Young Investigator Program Award N00014-21-1-2605. S. D. T. acknowledges support from the Army Research Office with Grant W911NF-22-2-0205. A. D. acknowledges support from the BTAA International Research Experience Program. J. P. S. also acknowledges Huntsman for carbon nanotube samples. The authors acknowledge Kyra Wilson for assistance in polishing the resin block for cross-sectional imaging.

References

1 R. F. Gibson, *Principles of Composite Material Mechanics*, CRC Press, Boca Raton, 4th edn, 2016.
2 T. Sai, S. Ran, Z. Guo, P. Song and Z. Fang, *SusMat*, 2022, **2**, 411–434.
3 X.-H. Shi, X.-L. Li, Y.-M. Li, Z. Li and D.-Y. Wang, *Composites, Part B*, 2022, **233**, 109663.
4 R. Liu, P.-f. Zhang, G.-T. Shen, Y. Zhang, W. Zhou, K.-M. Xiao and Q. Li, *Adv. Eng. Mater.*, 2023, **25**, 2201897.
5 N. Fantuzzi, A. Dib, S. Babamohammadi, S. Campigli, D. Benedetti and J. Agnelli, *Composites, Part C*, 2024, **14**, 100447.
6 W. Yang, J. Tan, J. Wang, W. Chang, M. S. Islam, Z. Sha, C. Wang, B. Lin, J. Zhang, G. H. Yeoh, C. Boyer and C. H. Wang, *Compos. Sci. Technol.*, 2025, **261**, 111005.
7 M.-Y. Shen, W.-Y. Liao and W.-T. Feng, *Mod. Phys. Lett. B*, 2023, **37**, 2340010.
8 M. Zhi, X. Yang, R. Fan, S. Yue, L. Zheng, Q. Liu and Y. He, *Polym. Degrad. Stab.*, 2022, **201**, 109976.
9 P. Xu, C. Gao, J. Ma, Y. Fang, Z. Wang, Z. An, U. Hwang, X. Yang, Y. Xu and S. Kim, *Eur. Polym. J.*, 2024, **220**, 113505.
10 O. Dagdag and H. Kim, *Polymers*, 2024, **16**, 3343.
11 J. Feng, L. Liu, Y. Zhang, Q. Wang, H. Liang, H. Wang and P. Song, *Exploration*, 2023, **3**, 20220088.
12 Y. Chen, H. Feng, R. Li, C. Zhang, Y. Ao and L. Shang, *Prog. Org. Coat.*, 2025, **208**, 109522.
13 B. Biswas and B. K. Kandola, *Polym. Adv. Technol.*, 2011, **22**, 1192–1204.
14 A. Schäfer, S. Seibold, W. Lohstroh, O. Walter and M. Döring, *J. Appl. Polym. Sci.*, 2007, **105**, 685–696.
15 Y.-C. Zhang, G.-L. Xu, Y. Liang, J. Yang and J. Hu, *Thermochim. Acta*, 2016, **643**, 33–40.
16 P.-X. Tian, Y.-D. Li, Z. Hu and J.-B. Zeng, *Mater. Today Chem.*, 2024, **36**, 101965.
17 D. Zhuo, R. Wang, L. Wu, Y. Guo, L. Ma, Z. Weng and J. Qi, *J. Nanomater.*, 2013, **2013**, 820901.
18 G. Huang, S. Wang, P. a. Song, C. Wu, S. Chen and X. Wang, *Composites, Part A*, 2014, **59**, 18–25.
19 W. Yang, J. Kim, P.-C. Su and J. Kim, *Composites, Part A*, 2024, **182**, 108192.
20 F. Luo, K. Wu, J. Shi and X. Du, *J. Mater. Chem. A*, 2017, **5**, 18542–18550.
21 X. Wang, L. Song, W. Pornwannchai, Y. Hu and B. Kandola, *Composites, Part A*, 2013, **53**, 88–96.
22 S. Araby, B. Philips, Q. Meng, J. Ma, T. Laoui and C. H. Wang, *Composites, Part B*, 2021, **212**, 108675.
23 X. Shi, S. Luo, X. Du, Q. Li and S. Cheng, *Polymers*, 2022, **14**, 3091.
24 X. Chen, F. Peng, C. Wang, H. Zhou, X. Lin, W. Liu and A. Zhang, *Appl. Surf. Sci.*, 2022, **576**, 151765.
25 X.-H. Shi, Y.-J. Xu, J.-W. Long, Q. Zhao, X.-M. Ding, L. Chen and Y.-Z. Wang, *Chem. Eng. J.*, 2018, **353**, 550–558.
26 X. Ji, Y. Mu, J. Liang, T. Jiang, J. Zeng, Z. Lin, Y. Lin and J. Yu, *Carbon*, 2021, **176**, 21–30.
27 H. Liu, Z. Huang, T. Chen, X. Su, Y. Liu and R. Fu, *Chem. Eng. J.*, 2022, **427**, 131540.
28 Y. Zhang, H. Feng, X.-F. Liang, S. He, J. Lan and L. Li, *Fish Shellfish Immunol.*, 2022, **121**, 265–275.
29 M. Hasan, Y. Patel, A. R. Gamboa, M. J. Grzenda, V. Saro-Cortes, V. Mhatre and J. P. Singer, *Adv. Mater. Interfaces*, 2022, **9**, 2200145.
30 X. Yao, T. P. Raine, M. Liu, M. Zakaria, I. A. Kinloch and M. A. Bissett, *J. Mater. Sci.*, 2021, **56**, 19538–19551.
31 R. Walvekar, S. Bhaumik, T. Nagarajan, M. Khalid, A. K. Rasheed, T. C. S. M. Gupta and V. Paleu, *Lubricants*, 2023, **11**, 71.
32 J. Yu, H. Wang, L. Kong, H. Zhu and Q. Zhu, *J. Nanomater.*, 2020, **2020**, 8725390.
33 A. V. Shchegolkov, A. V. Shchegolkov, V. V. Kaminskii, P. Iturralde and M. A. Chumak, *Polymers*, 2025, **17**, 71.
34 Y. Zhou, W. Qian, W. Huang, B. Liu, H. Lin and C. Dong, *Nanomaterials*, 2019, **9**, 1450.
35 Z. Wang, X. Shen, N. M. Han, X. Liu, Y. Wu, W. Ye and J.-K. Kim, *Chem. Mater.*, 2016, **28**, 6731–6741.
36 D. Mani, M. C. Vu, T.-H. Jeong, J.-B. Kim, C.-S. Lim, J.-H. Lim, K.-M. Kim and S.-R. Kim, *Composites, Part A*, 2021, **149**, 106585.
37 H. Zhang, X. Shen, E. Kim, M. Wang, J.-H. Lee, H. Chen, G. Zhang and J.-K. Kim, *Adv. Funct. Mater.*, 2022, **32**, 2111794.
38 M. C. Vu, I. H. Kim, W. K. Choi, C. S. Lim, M. A. Islam and S. R. Kim, *ACS Appl. Mater. Interfaces*, 2020, **12**, 26413–26423.

39 A. Nakayama, in *Advances in Heat Transfer*, ed. J. P. Abraham, J. M. Gorman and W. J. Minkowycz, Elsevier, 2023, vol. 56, pp. 51–111.
40 A. Toldy, G. Szebényi, K. Molnár, L. F. Tóth, B. Magyar, V. Hliva, T. Czigány and B. Szolnoki, *Polymers*, 2019, **11**, 303.
41 S. Shi, Y. Wang, T. Jiang, X. Wu, B. Tang, Y. Gao, N. Zhong, K. Sun, Y. Zhao, W. Li and J. Yu, *ACS Omega*, 2022, **7**, 29433–29442.
42 R. Si, D. Jing, F. Liu, D. Kong, X. Liu and J. Lu, *J. Phys.: Conf. Ser.*, 2023, **2539**, 012083.
43 S. Yasufuku, *IEEE Trans. Electr. Insul.*, 1982, **EI-17**, 338–344.
44 R. Januszewski, M. Dutkiewicz, H. Maciejewski and B. Marciniec, *React. Funct. Polym.*, 2018, **123**, 1–9.
45 S. Issazadeh, S. M. Seraji, M. J. Khan, H. Gan, L. C. Henderson and R. J. Varley, *Composites, Part B*, 2022, **232**, 109629.
46 J. J. Chruściel and E. Leśniak, *J. Appl. Polym. Sci.*, 2011, **119**, 1696–1703.